Solidification Behavior and Microstructure Formation in A Cast Nickel Based Superalloy: Experiment and Modeling

J. Zou¹, H. P. Wang², R. Doherty¹ and E. M. Perry²
 ¹ Department of Materials Engineering
 Drexel University, Philadelphia, PA 19104
 ² GE Research and Development Center
 Schenectady, NY 12301

Key Words: Superalloy, solidification, microstructure formation and modeling.

ABSTRACT

The solidification behavior of a nickel based superalloy (GTD-11111/) has been determined by using a modified DTA technique which allowed us to measure the liquidus, solidus and eutectic temperatures on heating and the maximum undercooling and the local solidification time, on cooling, obtained in each sample. The concentrations of alloy elements at the center and edge of dendrite arms and in the carbide and matrix phases have been determined by WDS microanalysis, which helped us to identify the phases formed during solidification. The partitioning of each alloy element has been studied by the average ratio of concentration at the center of dendrite arm against that at the dendrite edge. The grain sizes and dendrite arm spacings at different cooling rates were measured on lightly etched sections of the samples which had been solidified in the modified DTA cooling runs while the eutectic size was measured on the polished section of the samples. An empirical relationship between the maximum undercooling and the grain size has allowed us to establish a quantitative nucleation law based on a previous analysis used in cast iron, steel, cast aluminum and aluminum aerospace alloys. A general solidification microstructure model initially developed for the binary system has been modified for a multi-component system such as nickel based superalloys. This model predicts the microstructural parameters in the castings: grain size and its distribution, and the primary and secondary dendrite arm spacings, all as functions of the cooling rate. The predictions of this model compare well with the measured results. This model should be applicable to other superalloys.

^{1/} GTD-111 is a patented nickel-based superalloy by General Electric Co. (see Ref. [1]).

INTRODUCTION

The purpose of this work is to identify and predict quantitatively the solidification behavior and associated microstructure formation, during solidification, of a nickel-based superalloy, GTD-111, see Table I. GTD-111 has been developed and used as a mainstream superalloy for the buckets of land-based gas turbines in GE as reported in Ref. [1]. The gas turbines buckets are made by vacuum investment casting and by directional solidification techniques. The formation of the equiaxed grain structure during the vacuum investment casting has been investigated in this work. As reported by Schilke et al.[1], GTD-111 has a 20 °C (35 °F) creep-temperature advantage over IN-738, and a higher low-cycle fatigue strength. The identification of the solidification behavior and microstructure formation of GTD-111 superalloy is studied here by a modified DTA technique, by Optical and Scanning Electron Microscopy (SEM) and by microprobe and quantitative metallographical analyses. A mathematical model has been developed for quantitative simulation of the microstructure formation with regard to nucleation, growth and impingement of grains based on the identified solidification behavior and the measured microstructural parameters (e.g., cooling curve, distribution of alloy elements due to the microsegregation, grain size, Dendrite Arm Spacing / cell size (DAS) and eutectic spacing and size). This method and the mathematical model have been initially established by Rappaz and coworkers[2-4] and by Zou et al.[5-8] for cast aluminum casting alloy[2-4,6], cast iron[5], the a wrought aluminum aerospace alloy, 2024[7] and for a steel alloy[8].

Table I			Nominal composition of GTD-111 and IN-738 superalloys [1]										
[wt%]	Cr	Ni	Co	Fe	W	Mo	Ti	Al	Nb	С	В	Ta	
GTD-111	14	Bal	9.5	-	3.8	1.5	4.9	3.0	-	0.10	0.01	2.8	
IN-738	16	Bal	8.3	0.2	2.6	1.75	3.4	3.4	0.9	0.10	0.001	1.75	

EXPERIMENTAL METHODS

GTD-111 specimens were machined into cylindrical shapes with four different diameters of 10, 15, 25, 35 mm and a length of 30 mm. They were then placed into the alumina crucibles, 99.8% purity, having the same shape and sizes. A thermoucouple of Pt-6%Rh/Pt-30%Rh, type B, (wire: 0.2 mm; with two hole round Al₂O₃ insulators (2x0.4/1.6 mm) was placed at the center of each specimen in a hole of diameter of 2.0 mm and at depth of 15 mm. Another identical thermocouple was placed at the edge. In each run of the experiment, the four different sizes of the specimens were all placed in a graphite crucible as seen in Fig. 1. The graphite crucible was at the center of an induction coil in a vacuum furnace. The furnace was first evacuated and then back-filled with Ar gas (99.98% purity). The heating and cooling curves were recorded by an IBM PC. The thermocouples were calibrated by measuring the melting point and highest solidifying temperature during the heating-cooling of a pure nickel specimen (99.7% purity). The measured melting point was about 2.5±0.5°C lower than the standard melting point of pure nickel (1052.0°C). All thermocouples results used in this work were then adjusted by adding the additional 2.5°C. After solidification, the specimens were cut in half, and the cross section of each specimen was polished and etched for study by microscopy.

The liquidus, solididus and eutectic temperatures (T_I, T_S and T_e) were determined from the heating curves as shown in Fig. 2a,b. A discontinuity in the heating curve was taken as the temperature for carbide dissolution, T_c, but no sign of this transformation was seen on the cooling curves. The interdendritic location of the carbide phase in the microstructure indicates that the carbide is very unlikely to be first phase to solidify. T_c, may be a non-equilibrium, kinetic, carbide dissolution temperature but no further information on this has been yet obtained. The additional thermocouple at the edge of a specimen was used to determine more accurately the phase transformation temperatures through the temperature differential from the center to the edge. An example in the specimen of 35 mm diameter is shown in Fig. 2a. The electric power was held constant during heating for the range of temperatures shown in the figure but was completely cut off during cooling. The "carbide", liquidus, and solidus temperatures, but not the eutectic temperature, are seen in Fig. 2a. Oscillations during heating, Fig. 2a, might be caused by the turbulent motion caused by the induction heating. The average values of the carbide,

liquidus, and solidus temperatures were obtained over 17 measurements. There was, however, difficulty in determining the eutectic transformation temperature, Te, and it seemed that the eutectic arrest occurs over a range of temperatures. Only at a slow heating rate, 0.28 K/s, was the eutectic temperature clearly observed (see Fig. 2b). The average values of the carbide, liquidus, solidus and eutectic temperatures are noted in Table II. The maximum undercooling just before the recalescence, ΔT_{max} (see Fig. 6) is associated with the final grain density. The local solidification time, tf, associated with the primary and secondary dendrite arm spacings, was obtained by the corresponding cooling curve. tf is defined as the cooling time from the liquidus, T_I (1335 °C), to the eutectic, T_e (1094 °C). These thermal parameters are used later to predict the microstructural parameters.

Table II Average values of the carbide, liquidus, solidus and eutectic temperatures

			,		or action of
Tomporotura [OC]	T	Т.	Tr	T	
Temperature [°C]	1 _C	11	15	I e	
Omp 111	10.41	1000	1000	4004	
(†)-	1341	1445	1775	1094	
012	1371	1333	1413	1027	

Quantitative analysis of the microstructure was performed on the as polished and etched specimen surfaces as shown in Fig. 3a,b,c. As can be seen in Fig. 3a (etched surface), the grains are equiaxed and dendritic with the sizes of the order of millimeter (γ phase). The eutectic constituent is present between the primary and secondary dendrite arms (see Fig. 3b). In Fig. 3c (as-polished surface), the dark phase is the carbide phase (MC) and the rest is the matrix phase (dendritic γ phase). The grain size by volume, R_{ν} , in each specimen has been estimated from the number of grains per area, n_s, obtained from the whole cross section:

$$n_S \cdot \pi R_S^2 = 1$$
 and $R_V = \sqrt{(3/2)} \cdot R_S$ (1)

 $n_s \cdot \pi R_s^2 = 1$ and $R_v = \sqrt{(3/2)} \cdot R_s$ (1) The primary and secondary dendrite arm spacings were measured as the average straight distances between the primary dendrite arms and between the secondary arm spacings. The measurement of the size and the volume fraction of carbide and eutectic has not yet been completed. The composition of each phase has been determined by measuring the distribution of alloy elements using Wavelength Dispersive Spectrum (WDS) X-ray microprobe analysis. Examples of the distributions of Ta, Ti and Al scanning across a carbide particle are shown in Figs. 4a,b,c, respectively. Ta and Ti are enriched in the carbide phase MC (Fig. 4a,b) while Al is enriched in matrix / dendrite γ phase, (Fig. 4c). These type of solute distributions have been repeated over several carbide particles and consistent distributions were observed. The quantitative data of the major alloy elements have been obtained by the characteristic X-ray counts at different locations on the carbide and the matrix phases. These counts were converted into weight percent (as the uncorrected intensity ratios) by dividing the counts obtained on corresponding pure metal standards. Each measurement was repeated five times. The distributions of all major alloy elements in the secondary dendrite arms were also measured from the center to the edge. The ratio of concentration at the center of the dendrite to that at the edge is given as the relative solute partitioning of the element in the γ phase and the local ratios of element in in the carbide to that in the local y phase, are the MC ratios given in Table III. An example of the W distribution is given in Fig. 5.

Table III Relative solute partitioning in the matrix (\gamma\ phase) and the MC phases

	Cr	Ni	Co	W	Mo	Ti	Al	Ta	П
γ Phase MC Phase	1.146 0.200		1.013 0.072	1.290 1.800	0.887 1.000	0.786 1.800		0.642 2.500	

MODEL

GTD-111, in common with most superalloys, is a multi-component system but its phase diagram is unknown. A recorded cooling curve, instead, has been used to describe the solidification sequence as a function of solidification time, see Fig. 6. The melt cools linearly to the liquidus temperature. Below this temperature, the primary dendrite phase (y phase) first nucleates at heterogeneous nucleation sites and it then grows from an initially spherical shape into a dendritic shape. At the same time, new grains continue to nucleate until recalescence occurs until the heat released from the growth of grains matches the heat lost at the specimen surface. The nucleation of grains ceases once the recalescence occurs due to the decrease of the undercooling, see [2,5,6]. The dendritic grains soon impinge on each other and growth then stops. Thickening of dendrite arms continues until the temperature of the sample reaches the eutectic temperature. At the end of solidification a eutectic reaction occurs. Following the analysis of [2,5], the distribution of heterogeneous nucleation sites can be described by a normal distribution law and the density of grain nuclei at a given undercooling, $\Delta T(\tau)$, can be expressed

$$n(\Delta T(\tau)) = \frac{n_{\text{max}}}{\sqrt{2\pi} \cdot \Delta T_{\sigma}} \cdot \int_{\Delta T(t=0)}^{\Delta T(t=\tau)} \left(-\frac{\left(\Delta T(t) - \Delta T_{n}\right)^{2}}{2\Delta T_{\sigma}} \right) d(\Delta T(t))$$
(2)

where n_{max} is the maximum density of grain nuclei in the initial melt, ΔT_{σ} and ΔT_{n} are the undercoolings of the standard deviation and the center of the normal distribution of active heterogeneous nucleation sites [2,5]. Their values have been determined by the experiment. Once the grains have nucleated, they grow. The growth kinetics at the dendrite tip in a ternary system have been discussed in Refs. [4,9]. The growth theory has been redefined here in order to describe the growth kinetics at the dendrite tip in a more appropriate and quantitative way.

Liquidus temperature, $T_{lig}(\Sigma C_i)$:

$$T_{lig}(\Sigma C_i) = T_{l,o}(\Sigma C_{i,o}) + \sum m_i \cdot C_i$$
(3)

 $T_{liq}(\Sigma C_i) = T_{l,o}(\Sigma C_{i,o}) + \sum m_i \cdot C_i \tag{3}$ where $T_{l,o}(\Sigma C_{i,o})$ is the melting point of superalloy (e.g., GTD-111 superalloy in this work), C_i is the activity of atom i in the multi-component system which can be simplified as the concentration of element i if the interactions between the atoms are negligible, mi is the liquidus slope in the multi-component system corresponding the concentration C_i.

Total undercooling at a given growth rate, ΔT_{total} :

$$\Delta T_{\text{total}} = \sum \Delta T_{k,i} + \Delta T_{\text{th}} + \sum \Delta T_{c,i} + \Delta T_{r}$$
(4)

 $\Delta T_{total} = \sum \Delta T_{k,i} + \Delta T_{th} + \sum \Delta T_{c,i} + \Delta T_{r}$ (4) where $\Delta T_{k,i}$ is the kinetic undercooling associated with atomic attachment at the solid-liquid interface for the atoms of alloy element i, ΔT_{th} is the temperature difference due to thermal diffusion, $\Delta T_{c,i}$ is the undercooling due to solute diffusion of atoms of alloy element i and ΔT_r is the capillary undercooling due to the solid-liquid interface curvature. The kinetic and the thermal undercoolings are neglected in this work.

In the previous work[4,9], it was assumed that the capillary undercooling was so small that it could be neglected. For GTD-111 superalloy, there is no available experimental data of the solidliquid surface energy. The authors have estimated the solid-liquid interface energy of GTD-111 from the measured composition, partition coefficients and liquidus temperature slopes in GTD-111 and the empirical relationship of growth rate and primary dendrite arm spacing at a given thermal gradient when the leading solid-liquid interface just breaks up into a cellular structure in IN-738 superalloy[10]. It was found that the solid-liquid interface energy may vary from 370 to 4250 mJ/m² (the solid-liquid interface energy of pure nickel is 356 mJ/m²) and the corresponding Gibbs-Thomson coefficient, Γ, may vary from 3.7x10-5 to 42.5x10-5 cm K. The minimum value for the solid-liquid interface energy of GTD-111 has been used in this work.

Constitutional undercooling, $\sum \Delta T_{c,i}$:

$$\sum \Delta T_{c,i} = T_{liq}(\sum C_i) - T^* = \sum m_i (C_{o,i} - C_{l,i}^*)$$
 (5)

$$\Delta T_{\text{tot}} = \sum m_i \cdot C_{0,i} \cdot (1 - 1/(1 - (1 - k_i) \cdot I_v(P_{e,c,i}))) + 2\Gamma/r$$
 (6)

 $P_{e,c}$ is Peclet number of solute, $v \cdot r/2D_l$, v is the growth rate, I_v is the Ivantsov function, Γ is the Gibbs-Thomson coefficient and r is the radius of the dendrite tip.

A diffusion coefficient in Ni-19.7wt%Cr melt at 1600°C of 3.6·10⁻⁵ cm²/s has been reported[12] and this value has then been used in this work. The growth kinetics of the dendrite tip of GTD-111 superalloy calculated from Eq. (6) is shown in Fig. 7. The calculated growth rate is higher than those measured in the ternary systems[9,11] so it seems that this growth rate is overestimated, because the growth of dendrite tip in a multi-component system is expected to be slower than that in the ternary system. The authors believe that this might be due to an underestimate of the solid-liquid interface energy. Assuming that the grain grows in a spherical shape, the variation of the volume fraction of solid at a given time, $\Delta f_s(t)$, can be calculated[2,5]:

$$\Delta f_{s}(t) = \Delta (4\pi/3 \cdot n(t) \cdot R(t)^{3} \cdot f_{i}(t)) \tag{7}$$

 $= 4\pi/3 \cdot R(t)^3 \cdot f_i(t) \cdot \Delta n(t) + 4\pi \cdot n(t) \cdot f_i(t) \cdot R(t)^2 \cdot v(t) \cdot \Delta t + 4\pi/3 \cdot n(t) \cdot R(t)^3 \cdot \Delta f_i(t)$

where R is the radius of the equiaxed grain, n is the density of grains per volume, v is the growth rate at the dendrite tip, given by Eq. (6), and f_i is the internal volume fraction of solid within the equiaxed dendritic grain. The first term on the right side arises from the variation of density of grains, the second term from the growth of the grains and the third term from the thickening of the dendrite arms during the growth.

In a binary system, the internal fraction, f_i, can be obtained from the growth model of a whole equiaxed dendritic grain, see Rappaz and Thevoz[2], based on a solute balance within the grain. Their model has been successfully applied to an aluminum casting alloy, Al-7wt%Si[6]. However Rappaz and Thevoz's growth model for a binary system cannot be easily extended into a multi-component system because it requires knowledge of the constitutional undercooling of each alloy element which it is not possible to measure experimentally. As a result, the authors propose a new model based on the thermal balance within an equiaxed dendritic grain rather than that of solute. Based on the model of Dustin and Kurz[12] which is based on the thermal balance at the outside of the equiaxed dendritic grain, the authors propose a model of the thermal balance within the equiaxed dendritic grain as illustrated in Fig. 8:

$$\kappa \cdot (dT^2/dr^2 + 2/r \cdot dT/dr) + \partial q/\partial t = 0$$
 (8)

A general solution of Eq. (8) is

$$T(r) = A + B/r + C \cdot r^2 \tag{9}$$

The corresponding boundary conditions can be defined: at the center of the grain, r=0, dT/dr=0; at the grain boundary, $r=R_g$, $\kappa \cdot dT/dr=-\nu \cdot L_\nu$ and $T=T^*$ (see Fig. 7). The temperature distribution within the equiaxed dendritic grain, T(r), can be obtained from Eq. (9) where A, B and C are determined by the above three boundary conditions. After having determined the temperature distribution in the grain, the internal volume, f_i , can be obtained by integrating the fraction solid from the center to the edge if the distribution of volume fraction of solid in the equiaxed dendritic grain is assumed to be only a function of temperature as calculated by Scheil equation.

The coarsening of dendrite arms during solidification or Scheil equation in a multi-component system such as GTD-111 superalloy can be expressed as:

$$C_{l,i} = C_{o,i} \cdot (1 - f_s)^{-(1-k_i)}$$
(10)

and
$$T_{l,o}(\sum C_{0,i}) - T_{lio}(\sum C_{l,i}) = \sum m_i (C_{0,i} - C_{l,i})$$
 (11)

So we obtain:
$$T_{liq}(\Sigma C_{l,i}) = T_{l,o}(\Sigma C_{o,i}) - \sum m_i \cdot C_{o,i} \cdot (1 - (1 - f_s)^{-(1 - k_i)})$$
 (12)

RESULTS AND DISCUSSION

The thermal history, and in particular the amount of recalescence, is directly associated with the solidification behavior illustrated in Fig. 6. The microstructural parameters with regard to grain size, primary and secondary dendrite arm spacing can be determined from the cooling curves. The observed values are compared with the prediction of the model below. The measured cooling curves in the two specimens (diameter of 10 and 15 mm) are compared with those calculated by the present model as shown in Fig. 9. This figure indicates that the model can calculate, rather accurately, the cooling curves and in particular the shape and depth of the observed recalescence. The four stages of solidification (nucleation, growth of equiaxed dendritic grains, coarsening of dendrite arms and eutectic solidification) illustrated in Fig. 6 can be predicted quantitatively by this model.

The Scheil equation has been widely used to estimate the solid fraction at a given temperature, so it is useful to compare our model with Scheil equation (see Fig. 10). The liquidus temperature

calculated from Eq. (12), the multi-component Scheil equation, ends near to the observed eutectic temperature, T_e = 1094 °C. The present model reports behavior close to that predicted by Scheil equation except at the early stages of the solidification, at a solid fraction less than 0.15. The Scheil equation is only valid when the whole specimen is fully filled by the dendrites. This situation is only found after the end of the recalescence, see Fig. 6. For this reason during the early stage of the solidification, the volume fraction of solid behaves totally differently from that estimated by the Scheil equation for a given temperature (see Fig. 10). During this stage of solidification, i.e. the nucleation and growth of equiaxed dendritic grains, the solid fraction increases not only by the thickening of dendrite arms within the grains but also by the increase of the grain size and the number of grains during recalescence, Eq. (7). For the rest of the solidification range after recalescence when the dendritic grains have filled the sample, so that solidification then takes place solely by the thickening of the dendrite arms, the prediction of our model reduces to the the multi-component Scheil equation. The validity of the expressions of Eqs. 7,12 appears to be justified by the good comparison of the predicted cooling curves with those measured, see Fig. 9. The measured and predicted primary and secondary DAS as a function of local solidification time are shown in Fig. 11. These predictions are quite simple. The proportionality constants between the local solidification time and the primary and secondary dendrite arm spacings are determined from the experimental data. When the heat flow leaving the specimen surface is known, the total solidification time can be obtained by the heat balance which was used to calculate the dendrite arm spacings.

The measured and predicted grain sizes as a function of solidification time are shown in Fig. 12. The model seems to predict the most general trend of the variation, but the predicted values are consistently higher than those measured so there is some factor in the measured values not captured by our model. One explanation of the failure is that the estimated heat flow leaving the specimen surface may not be accurate enough, indicating the need for an additional thermocouple at the edge of the specimen to obtain the exact heat flow leaving the surface (for more detail see Ref. [5]). A second hypothesis is that the calculated growth kinetics of grains (see Fig. 7) may be based on an underestimate of the solid-liquid surface energy (see the paragraph below Eq. (4)) or by the neglect of atomic attachment kinetics at the solid-liquid interface. If a higher value of the solid-liquid interface energy had been adopted, the equiaxed dendritic grains would have grown more slowly and this would have delayed the recalescence giving a deeper undercooling and producing a smaller predicted final grain size. More work is clearly needed for the grain size studies.

CONCLUSIONS

The primary dendrite, the carbide phase and the phases formed by the eutectic reaction during solidification have been identified as has the partitioning of each alloy element. A mathematical model was developed to describe the formation and evolution of the microstructure. The predicted cooling curves, recalescence and primary and secondary dendrite arm spacings match the measured values, while the grain sizes are less well described by the present model. Since there are no special restriction made on this model, it should be applicable to other superalloys.

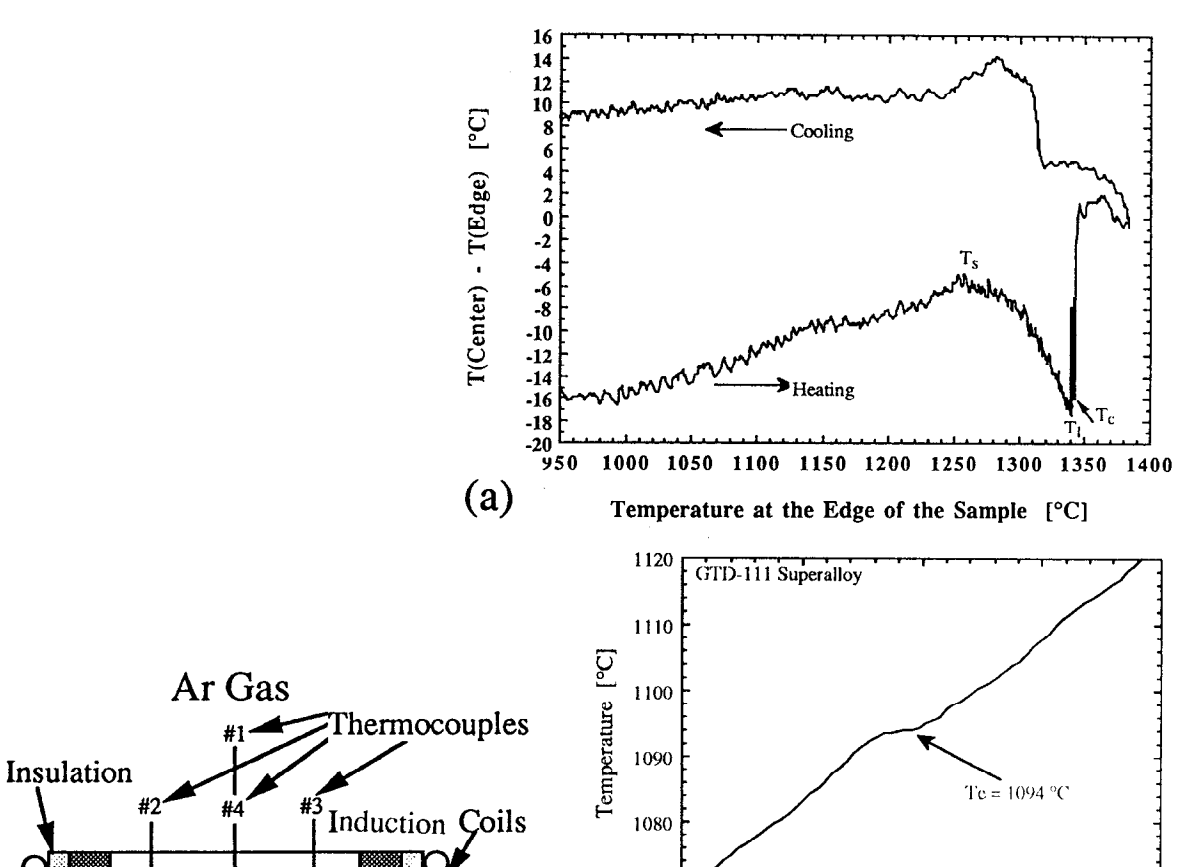
ACKNOWLEDGEMENTS

The authors would like to gratefully acknowledge the financial support of General Electric Co. for this research work. The authors would like to thank, in particular, A. Beltran and V. Kallianpur from GE Power Generation, for constant support and stimulating discussions. This project is a part of an on-going research program at GE.

REFERENCES

- 1. P. W. Schilke, A. D. Foster, J. J. Pepe and A. M. Beltran: <u>Advanced Materials Processes</u>, April 1992, 22-30.
- 2. M. Rappaz and Ph. Thévoz: Acta Metall. 35 (1987) 1487-97; 2929-2933.
- 3. Ph. Thévoz, J. L. Desbiolles and M. Rappaz, Metall. Trans. 20A (1987) 311.
- 4. Ph. Thévoz, J. L. Desbiolles and M. Rappaz, <u>Light Metals 1990</u>, Ed. C. M. Bickert (TMS Publ., Warrendale, PA, 1990) 975-984.

- 5. J. Zou and M. Rappaz: Materials Processing in The Computer Age, Eds. V. Voller et al., TMS (1991) 335-348, 349-360.
- J. Zou, S. Shivkumar and D. Apelian, <u>AFS Trans.</u> 99 (1991) 871-878.
- J. Zou and R. Doherty, Drexel University, Philadelphia, PA, Annual Report to Alcoa Technical Center, Sept. 1991.
- J. Zou and A. A. Tseng, Metall. Trans. 23A (1992) 457-468.
- M. Bobadilla, J. Lacaze and G. Lesoult, <u>J. Crystal Growth</u> 89 (1988) 531-544.
 P. N. Quested and M. McLean, <u>Mater. Sci. and Engin.</u>, 65 (1984) 171-180.
- 11. J. Lacaze, A. Chehaibou and G. Lesoult, Z. Metallkde 80 (1989) 15-20.
- 12. I. Dustin and W. Kurz, Z. Metallkde 77 (1986) 265-273.
- 13. Diffusion and Defect Data, 8 (1974) p.141.
- 14. K. O. Yu et al., AFS Trans. 98 (1990) 417-428.



00000000000 1070 1800 1850 1900 1950 2000 (b) Time [s] Fig. 2 a) Differential temperature between the center and the edge of the specimen during the heating-cooling processes and the carbide, liquidus and solidus temperature, T_c, T_l and T_s; Graphite b) The measured eutectic temperature, T_e.

Fig. 1 Schematic of the experiment apparatus.

Ceramics

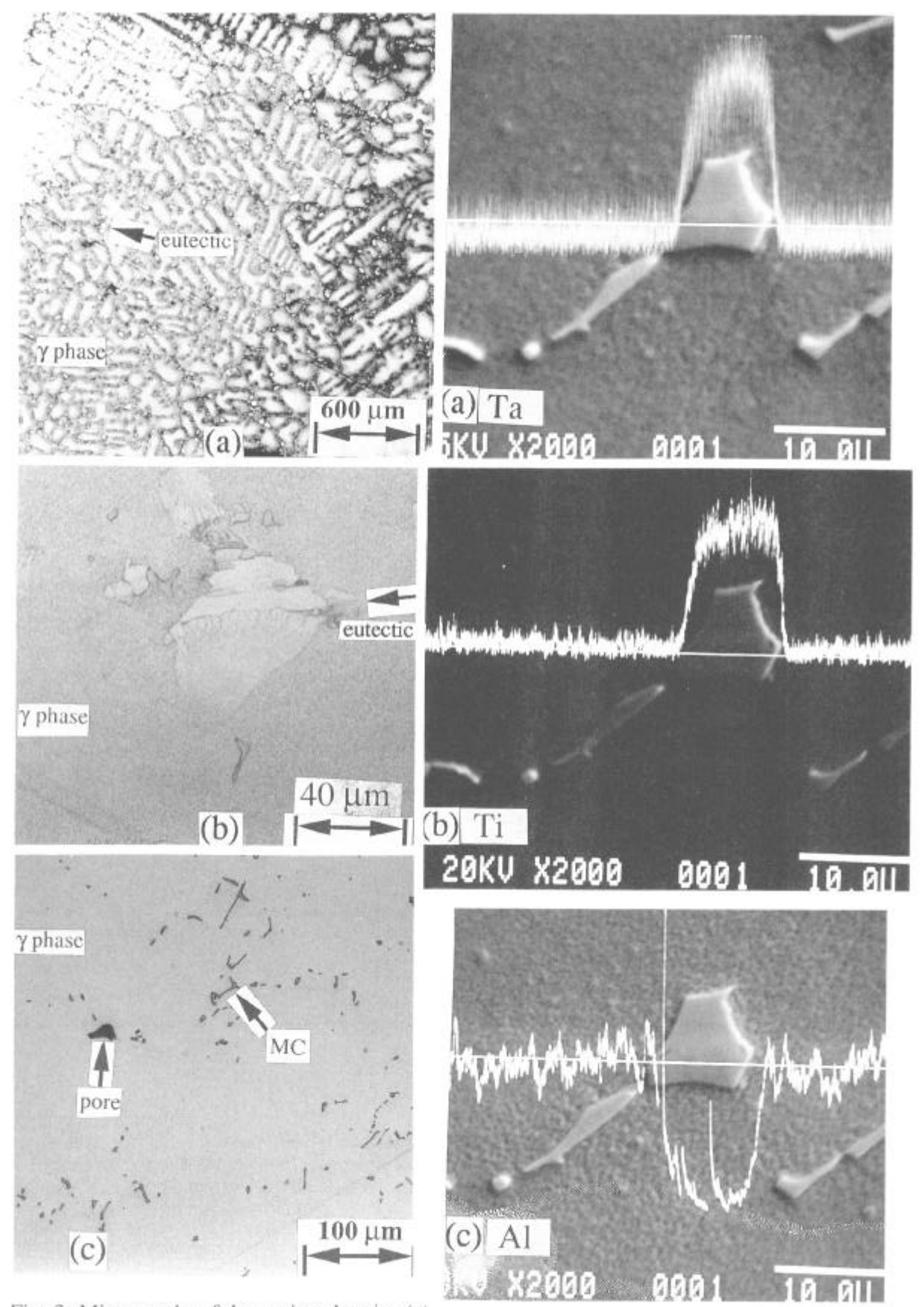


Fig. 3 Micrographs of the equiaxed grains (a) and eutectic phase (b) on the etched surface and Fig. 4 Microsegregation of Ta (a), Ti (b) and Al the carbide particles (c) on as polished surface. (c) in MC particle and matrix phase (γ phase)

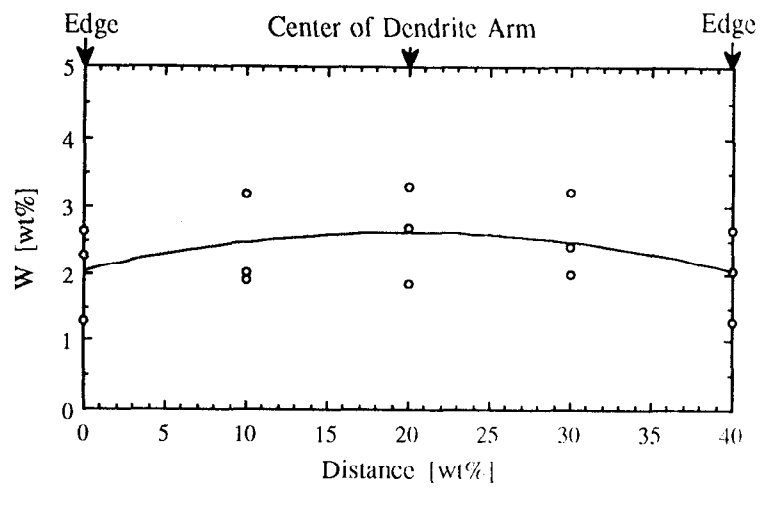


Fig. 5 Microsegregation of W from the center to the edge of the dendrite arms (y phase).

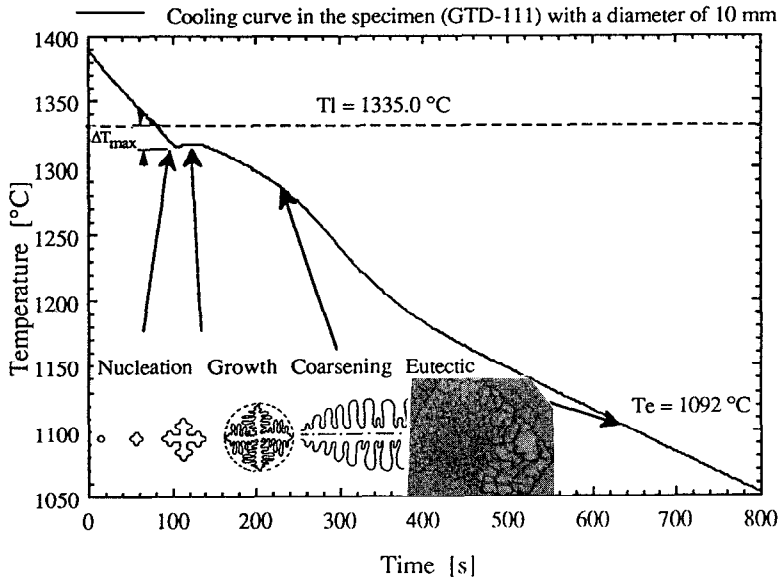
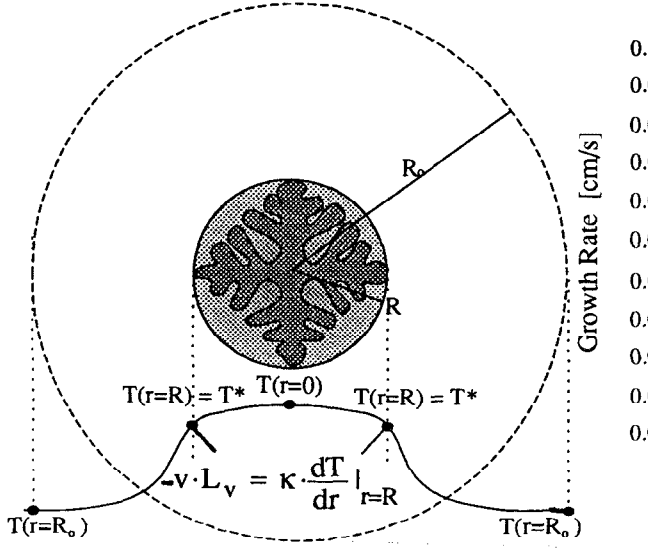


Fig. 6 Solidification sequence of GTD-111 superalloy.



0.10 Cal. growth kinetics of CTD-111

O Mes. Ni-7.2wt%Al-6.4wt%Ta [10]

Mes. Fe-18.4wt%Cr-12.4wt%Ni [9] 0.09 0.08 0.07 0.06 ΔTc,i+ΔTr 0.05 0.04 0.03 0.02 0.01 3 5 6 7 8 9 10 11 12 13 14 15 2 Undercooling [°C]

Fig. 7 Growth kinetics at a dendrite tip of GTD- Fig. 8 Schematic of equiaxed dendritic grain 111 superalloy.

growth and its temperature distribution.

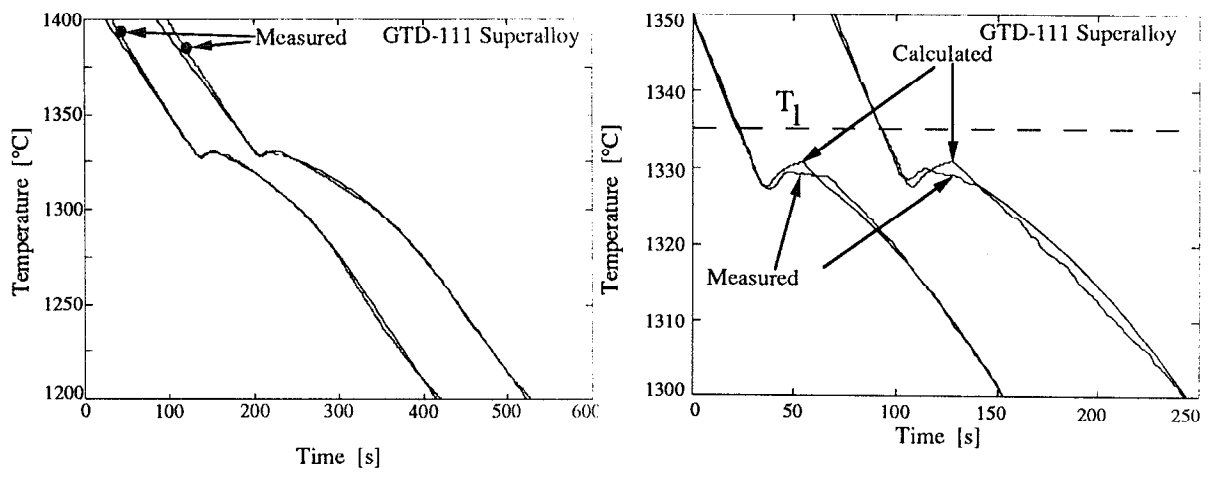


Fig. 9 Measured and calculated cooling curves in the two specimens (diameter of 10 and 15 mm).

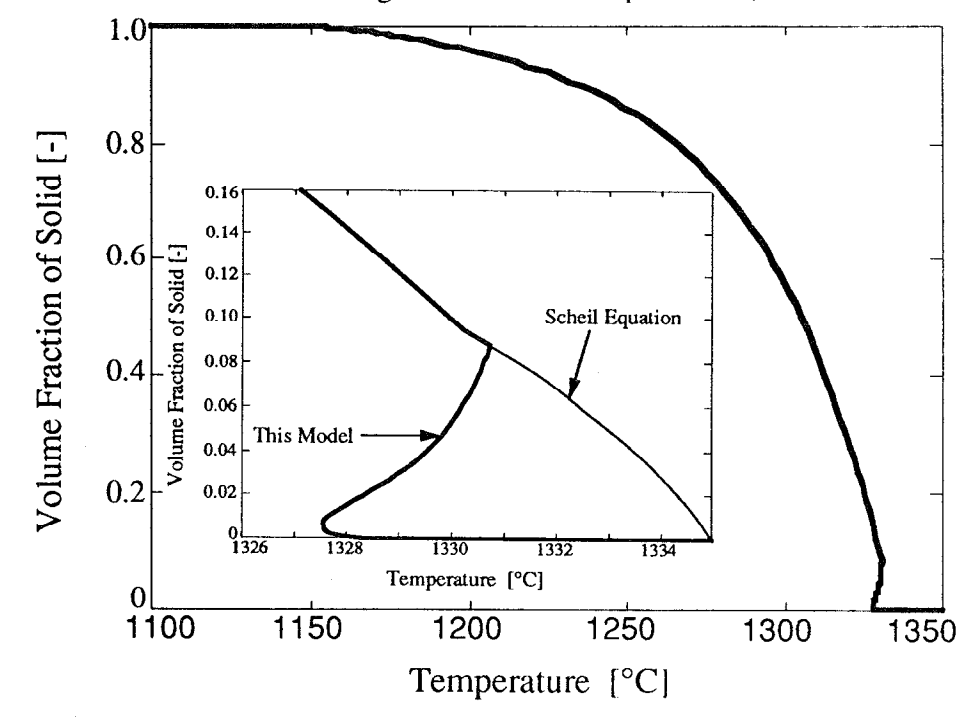


Fig. 10 Scheil equation in GTD-111 superalloy.

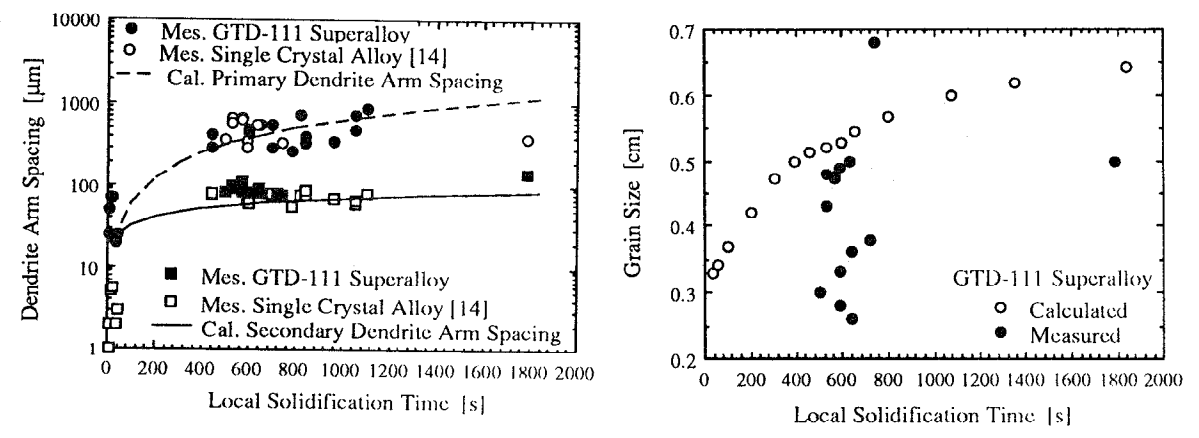


Fig. 11 Measured and predicted grain size as Fig. 12 Measured and predicted primary and function of local solidification time.

secondary DAS as function of solidification time.